CELL BIOLOGY

Osteoblastic lysosome plays a central role in mineralization

Tomoaki Iwayama[1]*, Tomoko Okada[2]*, Tsugumi Ueda[1], Kiwako Tomita[1], Shuji Matsumoto[1], Masahide Takedachi[1], Satoshi Wakisaka[3], Takeshi Noda[4], Taku Ogura[5], Tomomichi Okano[5], Peter Fratzl[6], Toshihiko Ogura[2]†, Shinya Murakami[1]†

Mineralization is the most fundamental process in vertebrates. It is predominantly mediated by osteoblasts, which secrete mineral precursors, most likely through matrix vesicles (MVs). These vesicular structures are calcium and phosphate rich and contain organic material such as acidic proteins. However, it remains largely unknown how intracellular MVs are transported and secreted. Here, we use scanning electron-assisted dielectric microscopy and super-resolution microscopy for assessing live osteoblasts in mineralizing conditions at a nanolevel resolution. We found that the calcium-containing vesicles were multivesicular bodies containing MVs. They were transported via lysosome and secreted by exocytosis. Thus, we present proof that the lysosome transports amorphous calcium phosphate within mineralizing osteoblasts.

INTRODUCTION

Bone mineralization refers to the physiological deposition of calcium phosphate crystals in the extracellular matrix, and it is one of the most fundamental processes in all vertebrates (1, 2). Already in 1967, Anderson (3) and Bonucci (4) individually visualized mineral-related particles in extracellular space via electron microscopy (EM), which were later recognized as mineralizing nanovesicles or matrix vesicles (MVs). Despite over 50 years of EM studies on MVs, the mechanism of how MVs are produced and secreted remains largely unknown (5–8).

It has been challenging to clarify mineralizing processes of live cells with EM because sample preparation for EM requires chemical fixation and alcoholic dehydration that may produce artifacts by dissolving and removing unstable mineral precursors, leaving behind an organic scaffold that has been coined "crystal ghost" (9, 10). While EM using fixed and dehydrated tissue has been used successfully to image the structure of mineralized collagen fibrils in bone (11, 12), cryo-EM approaches are needed to study mineral precursors, since this avoids dehydration but requires extremely fast cooling with small specimens (13, 14).

RESULTS AND DISCUSSION

To overcome these limitations, we used a novel microscopic system, scanning electron-assisted dielectric microscopy (SE-ADM), wherein both nanoscale resolution and high-contrast imaging were achieved for mammalian cells in aqueous media without staining (15, 16). Here, we explored the possibility of visualizing MVs in intact osteoblasts with high-resolution SE-ADM with the aim of clarifying the biogenesis and trafficking of MVs. The system setup for observing osteoblastic MVs is illustrated in fig. S1A. As an osteoblast cell line, we used the murine osteoblastic cell line KUSA-A1, which has a high osteogenic capacity in vitro and in vivo (17). The cells stably expressed transcription factors necessary for osteoblast differentiation (fig. S1B). When the cells were cultured with ascorbic acid and phosphate for 3 days, calcified nodules formed as revealed through Alizarin Red S staining (fig. S1C). Using an optical phase-contrast microscope, we first confirmed that cells in culture successfully formed a monolayer attached to the thin SiN film (fig. S1D) in the SE-ADM system, proliferated, and differentiated to form calcified nodules on the film (fig. S1E). Thereafter, high-resolution SE-ADM was performed to observe cells in culture (fig. S1A), and normal intracellular structures were identified (15). The cells in the confluent monolayer were further cultured in normal or osteogenic media containing ascorbic acid and phosphate. At an early stage of differentiation (day 2), black particles were present when cultured in osteogenic media (Fig. 1A, right), but not in normal media (Fig. 1A, left). The particles seemed to be contained in vesicles (Fig. 1A, right). At a later stage (after 7 days culture), numerous particles were visible when cultured in osteogenic media, although not in normal media (Fig. 1B). To determine whether they were localized in the intracellular or extracellular space, we manually detached the cell monolayer from the film, using forceps, and observed the film again. High-resolution SE-ADM observation of the remaining film revealed that most particles were firmly attached to the film (Fig. 1C, right), which is concurrent with previous reports that the secreted MVs are located in the narrow gap between collagen fibrils (18). Observation of MVs at later stages revealed that MVs were ubiquitously distributed (Fig. 1C, right) with some tendency to align to collagen fibrils (fig. S2, A to C). To analyze the size of these secreted particles, we used SE-ADM after 4 to 10 days of culture in osteogenic media (Fig. 1D). Secreted particles increased their size during the osteogenic culture (Fig. 1E), suggesting fusion or particle growth. When we measured the size of 900 to 1100 particles on the image for each and calculated the diameter, the average particle size was 98 nm on day 4 and gradually increased to 117 nm on day 7 and 223 nm on day 10 (Fig. 1E). The particles observed in osteogenic media ranged from 4 to 320 nm, with a median size of 90 nm, which was consistent with the previously reported size of MVs (6, 8), suggesting that they are indeed MVs. However, we cannot rule out the possibility that these particles precipitated spontaneously in the extracellular space after secretion from the cell.

[1]Department of Periodontology, Osaka University Graduate School of Dentistry, Suita, Osaka 565-0871, Japan. [2]Biomedical Research Institute, National Institute of Advanced Industrial Science and Technology (AIST), Tsukuba, Ibaraki 305-8566, Japan. [3]Department of Oral Anatomy and Development, Osaka University Graduate School of Dentistry, Suita, Osaka 565-0871, Japan. [4]Center for Frontier Oral Science, Graduate School of Dentistry, and Graduate School of Frontier BioSciences, Osaka University, Osaka 565-0871, Japan. [5]Lion Corporation, Tokyo 132-0035, Japan. [6]Department of Biomaterials, Max Planck Institute of Colloids and Interfaces, Potsdam-Golm 14476, Germany.
*These authors contributed equally to this work.
†Corresponding author. Email: t-ogura@aist.go.jp (To. Ogura); ipshinya@dent.osaka-u.ac.jp (S. Mu.)
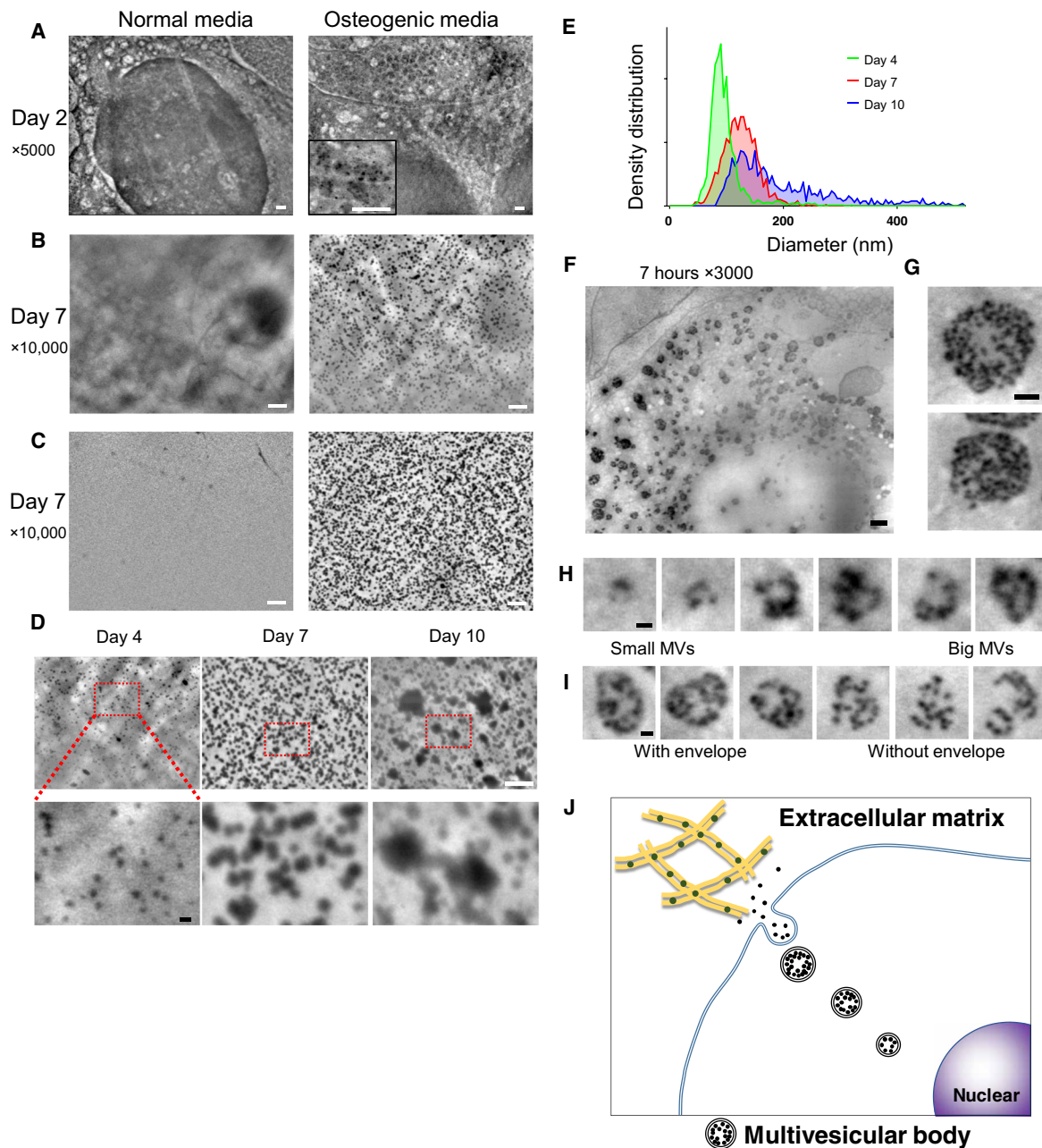
Fig. 1. Nanoscale observation of live osteoblasts in culture media, using the SE-ADM system. (**A**) Representative high-resolution SE-ADM images of osteoblasts cultured with or without osteogenic media for 2 days. Black particles were evident only when cultured in osteogenic media (right, square in the bottom). (**B**) Representative high-resolution SE-ADM images of osteoblasts cultured with or without osteogenic media for 7 days. There are many black particles when cultured in osteogenic media (right). (**C**) Representative high-resolution SE-ADM images of the SiN film after cell removal. In normal media, no particles are observed (left). The image of the film after removal of cells cultured in osteogenic media shows many clear black particles dispersed in the whole area (right). (**D**) Comparison of particle images during 4 to 10 days of culture in osteogenic media. The particle sizes gradually increased. (**E**) Distribution of particle size measured during 4 to 10 days of culture in osteogenic media. Approximately 900 to 1100 particles per time point were measured and plotted as a histogram. (**F**) Representative high-resolution SE-ADM images of osteoblasts cultured with osteogenic media for 7 hours. (**G**) MVBs have clear gray envelopes. (**H**) Cut images of various MVB sizes, including particles. (**I**) Comparison of MVBs with or without a gray envelope. (**J**) Schematic view of intracellular formation and transport of MVB in mineralizing osteoblasts. Scale bars, 1 μm in (A) to (C) and (F); 500 nm in (G); 200 nm in (D, bottom), (H), and (I).

To investigate how these particles were generated and secreted, we performed the SE-ADM analysis 7 hours after changing the osteogenic media (Fig. 1F). Through careful observation of these particles, we found that they gathered together in vesicles as seen in Fig. 1F and had clear gray envelopes around 1.5 μm in diameter (Fig. 1G), which seemed similar to multivesicular bodies (MVBs) encapsulating exo-

somes (*19*). Furthermore, structures of different sizes were observed (Fig. 1, H and I, and fig. S2D), thereby strongly suggesting that MVs gathered in MVB and grew in size with an increase in number. The mechanisms underlying MV secretion are controversial. Most reports suggest that MVs are secreted via budding from the plasma membrane (*20*), whereas other mechanisms have also been suggested,

including exocytosis (21). We also observed MVB structures with no gray envelopes (Fig. 1I). These observations suggest the involvement of the lysosomal pathway in transporting and secreting intraluminal MVs (Fig. 1J), similarly to exosomes (19). Exosomes and MVs are both categorized as extracellular vesicles with similar sizes, and it has recently been suggested that they are both secreted by osteoblasts and may share functions in cell-cell communication (8). Recent evidence showed that calcium phosphate in the cytosol exists in an amorphous state, and formation of a first calcium phosphate mineral (nucleation) is needed for initiating crystallization (9, 14, 22, 23). The process is known to be a pH dependent (24); calcium phosphate can be crystallized in neutral to basic pH. Lysosomes are the cell's degradation center (25) and recognized as "acidic Ca^{2+} stores" (26). However, the role of lysosomes in bone mineralization has not been investigated.

We further investigated whether these particles are MVs containing calcium and/or phosphate. The cells were cultured in osteogenic media for 7 days and observed by SE-ADM (Fig. 2A). Subsequently, the SiN films were observed after cell removal: our pseudocolor maps of SE-ADM observation showed a very smooth structure without crystal facets (Fig. 2B, right), suggesting that minerals in the MVs did not crystallize but remained amorphous, which is consistent with a previous report showing that mineral precursors in vertebrate bones are amorphous calcium phosphate (23). The energy-dispersive x-ray (EDX) spectrometric analysis of the MVs on a SiN film revealed that the particles in the osteogenic media had sharp peaks in phosphorus and calcium (Fig. 2C, right, yellow arrows), while there were no peaks in the normal media (Fig. 2C, left). The particles contained phosphorus, calcium, carbon, and oxygen (Fig. 2D), suggesting that the particles were constructed by calcium phosphate with proteins, which is in agreement with previous reports showing that MVs contain a variety of proteins (27). This analytical finding was further confirmed using Raman microscopy, which revealed a peak around 960 cm^{-1} (Fig. 2E, right), that is consistent with the v1 phosphate vibration (28). These results indicated that the particles within MVBs were calcium phosphate containing MVs.

Tissue-nonspecific alkaline phosphatase, encoded by the *Alpl* gene, is one enzyme anchored to the plasma membrane of osteoblasts and the surface of MVs, and it is responsible for hypophosphatasia (29). Osteoblasts from either patients or knockout mice have shown no mineralization in vitro (30, 31). Using CRISPR-Cas9, we generated *Alpl* knockout osteoblast clones (fig. S3, A to F). On high-resolution SE-ADM analysis of knockout clones with or without osteoblastic induction, no MVs were observed under both conditions (Fig. 2F). EDX spectrometric analysis confirmed that there were no clear peaks for phosphorus and calcium (Fig. 2G, right). These results further confirmed that the intraluminal vesicles in MVBs were MVs.

Having directly observed how MVs were generated and secreted, we then investigated the involvement of lysosome in intracellular trafficking of MVs in conjunction with fluorescent probes to observe live mineralizing osteoblasts. As an intracellular calcium phosphate probe for fluorescent imaging, we used the membrane-impermeable calcium binding fluorescent probe calcein. It has been used for labeling calcium phosphate in vivo and in vitro to identify mineral deposition (32, 33) but not for intracellular nanoscale imaging. Calcein labeling of osteoblasts showed that calcein-containing vesicles became brighter when cultured in osteogenic media (fig. S4A), and crystallized structures corresponded with Alizarin Red S staining (fig. S4B). The cells were cultured with calcein-containing osteogenic media

and stained with fluorescent LysoTracker which is a cationic dye that preferentially accumulates in acidic lysosome. The localization of calcein-fulfilled vesicles was matched with lysosomes (Fig. 3A, left, insets). To validate lysosome involvement in mineral trafficking, cells under osteogenic culture conditions were treated with a lysosomal proton adenosine triphosphatase inhibitor, bafilomycin A1 (BafA). Lysosomal acidification was completely abolished as reported (34), and distribution of calcein+ vesicles was markedly restricted within the intracellular space (Fig. 3A). SE-ADM observation in the same condition showed no electron-dense granules (Fig. 3B), suggesting that biogenesis of MVs was held in lysosomes after their fusion with calcein+ vesicles. Subsequently, we examined the effect of lysosomal exocytosis inhibitors to understand the secretion mechanism of MVs, which has been suggested as budding (20). When the cells were treated with an exocytosis inhibitor, vacuolin-1 (Vac-1), lysosomes were restricted within the intracellular space, and the pattern matched the increased calcein signal when treated (Fig. 3C). With Vac-1, MVBs were seen under SE-ADM (Fig. 3D), suggesting that their secretion via exocytosis, but not their biogenesis, was inhibited. Since the mode of actions of Vac-1 may be cell type dependent (35), we also used another inhibitor of lysosomal exocytosis, endosidin 2 (ES2), which targets the exocyst complex subunit (36). A similar intracellular accumulation of both lysosomes and calcein signals was confirmed when cells were treated with ES2 (fig. S4C). Last, we examined whether calcified nodule formation was blocked by inhibitors. Cells treated with both BafA and Vac-1 failed to form extracellular calcified nodules (Fig. 3E).

Mitochondria have been proposed to be involved in mineralization (9, 37–39). Electron-dense, Ca-, and P-rich granules were identified within cultured osteoblast mitochondria if samples were processed with a modified cryotechnique (9). Direct contact of mitochondria and lysosome has also been recently reported with functional significance (40). The cells were stained with LysoTracker together with MitoTracker and observed under N-SIM Structured Illumination super-resolution microscopy (SRM). We found that the most calcein-fulfilled vesicles were next to mitochondria and matched with lysosomes (Fig. 4A). We then performed SRM time-lapse imaging and found that LysoTracker containing vesicles fused to static calcein-containing vacuoles adjacent to mitochondria and then transported toward the periphery (Fig. 4B and movie S1). Furthermore, colocalization of transgenic LAMP1, lysosomal resident marker protein, and fused mCherry and calcein vesicles was confirmed (Fig. 4C).

Together with observations of the other SRM system or other cell line (fig. S4, D and E), we propose a mineralization mechanism where lysosomes play a central role in intracellular MV biogenesis and trafficking within osteoblasts (Fig. 4D). The involvement of lysosomes seems reasonable for cells to transport amorphous calcium phosphate without crystallization during its transport in the cytosol. Further experiments are needed to determine the regulatory molecules for MVs and to investigate whether MVs and exosomes have similar components and/or mechanisms underlying their generation and secretion. Our SE-ADM can be installed into existing scanning electron microscopy (SEM) at a low cost and offers nanoscale high-resolution imaging in a noninvasive manner, which can be applicable to all scientific fields.

MATERIALS AND METHODS
Cell culture and osteogenic differentiation
KUSA-A1 mouse osteoblastic cell line was obtained from JCRB Cell Bank (Japanese Collection of Research Bioresources Cell Bank;
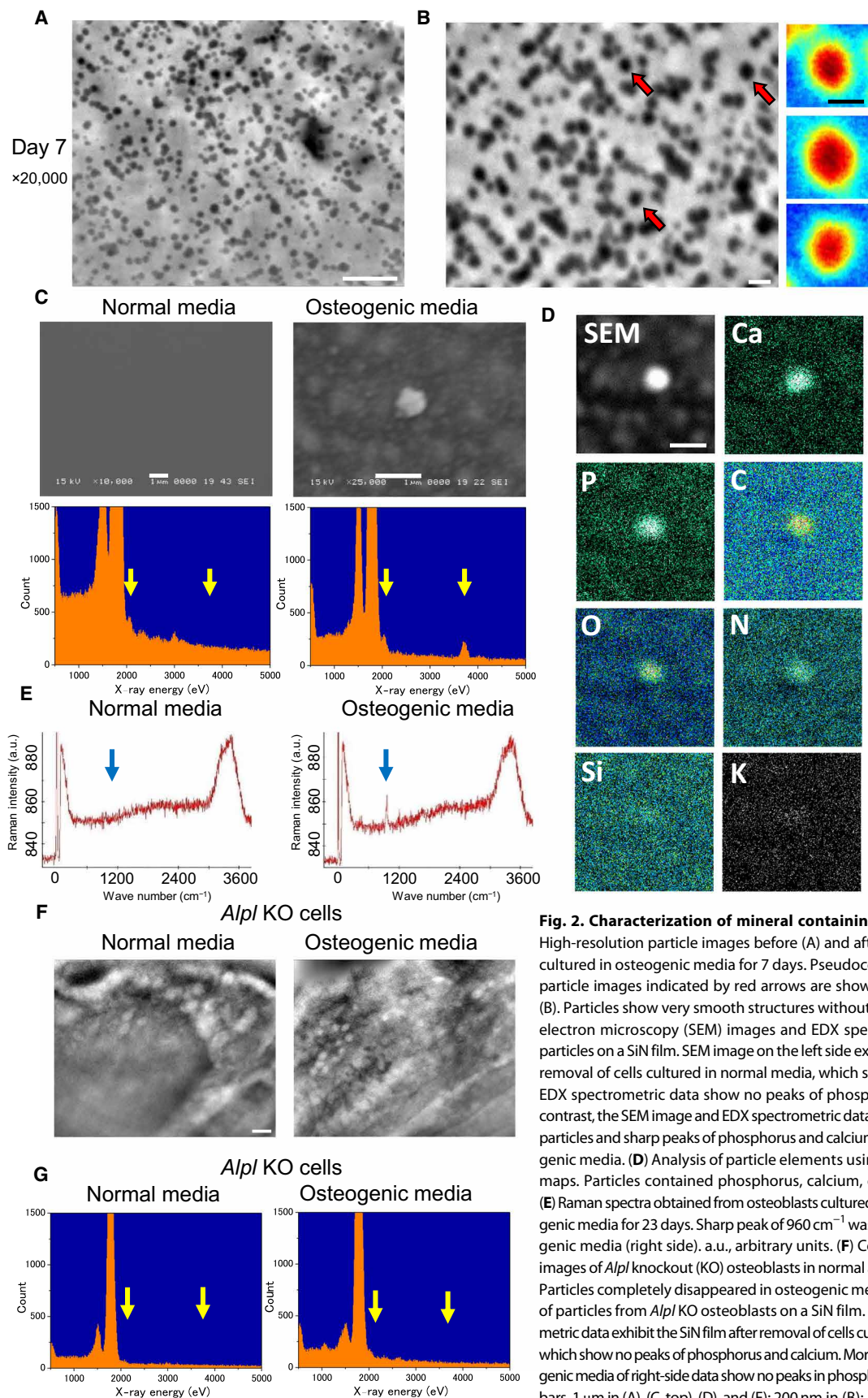
Fig. 2. Characterization of mineral containing vesicles. (**A** and **B**) High-resolution particle images before (A) and after (B) removal of cells cultured in osteogenic media for 7 days. Pseudocolor maps of enlarged particle images indicated by red arrows are shown on the right side of (B). Particles show very smooth structures without crystals. (**C**) Scanning electron microscopy (SEM) images and EDX spectrometric analysis of particles on a SiN film. SEM image on the left side exhibits the SiN film after removal of cells cultured in normal media, which shows no particles, and EDX spectrometric data show no peaks of phosphorus and calcium. In contrast, the SEM image and EDX spectrometric data on the right side show particles and sharp peaks of phosphorus and calcium after culture in osteogenic media. (**D**) Analysis of particle elements using EDX spectrometric maps. Particles contained phosphorus, calcium, carbon, and nitrogen. (**E**) Raman spectra obtained from osteoblasts cultured with or without osteogenic media for 23 days. Sharp peak of 960 cm^{-1} was evident only in osteogenic media (right side). a.u., arbitrary units. (**F**) Comparison of SE-ADM images of *Alpl* knockout (KO) osteoblasts in normal and osteogenic media. Particles completely disappeared in osteogenic media. (**G**) EDX spectrum of particles from *Alpl* KO osteoblasts on a SiN film. Left-side EDX spectrometric data exhibit the SiN film after removal of cells cultured in normal media, which show no peaks of phosphorus and calcium. Moreover, particles in osteogenic media of right-side data show no peaks in phosphorus and calcium. Scale bars, 1 μm in (A), (C, top), (D), and (F); 200 nm in (B); 100 nm in (B, right).
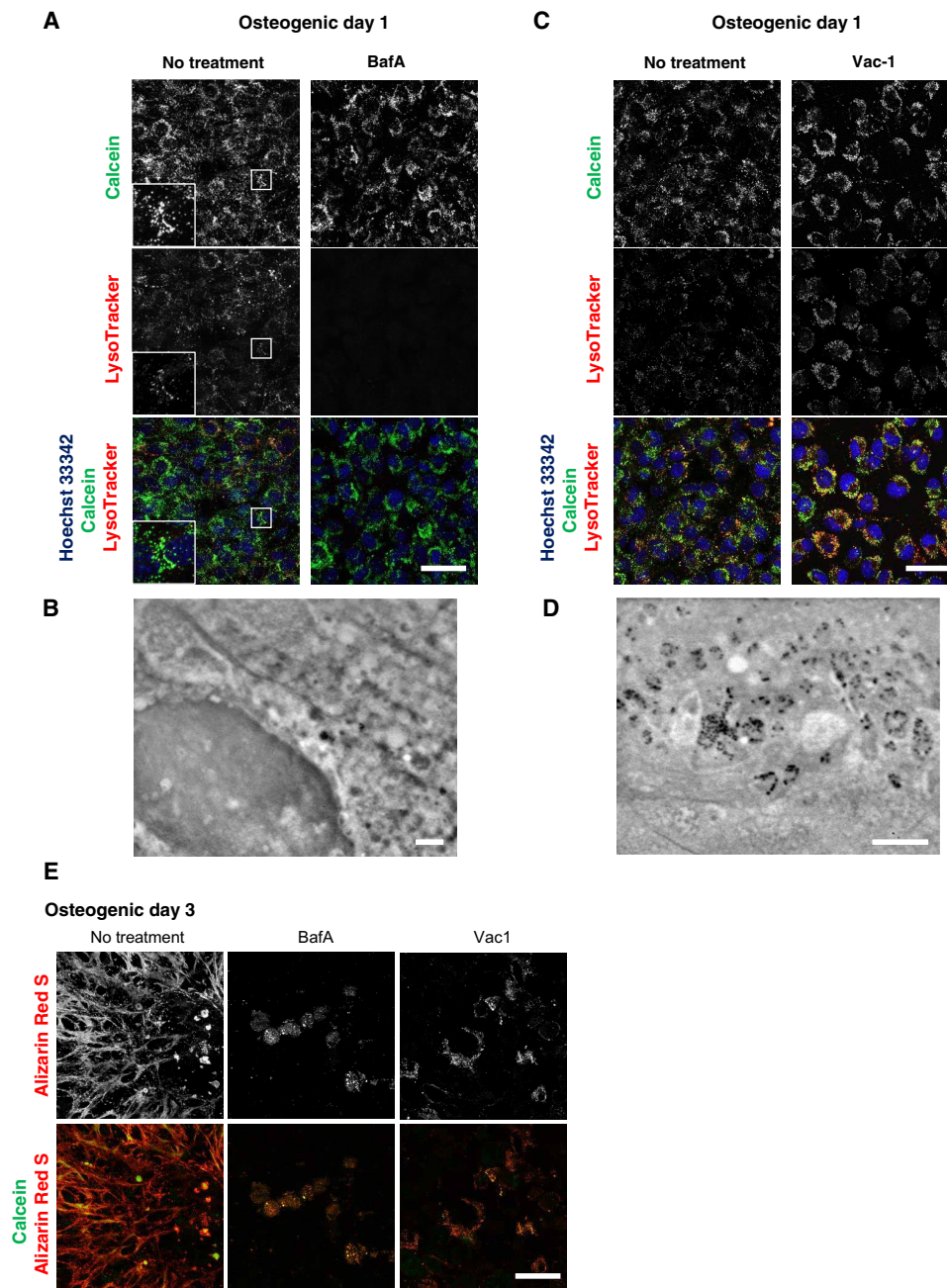
Fig. 3. Lysosomal inhibitors block mineralization. (**A** and **C**) Confocal live imaging of 50 nM BafA-or 10 µM Vac-1–treated osteoblasts. Cells were cultured in osteogenic media containing BafA or Vac-1 and stained with Hoechst 33342 and LysoTracker Insets show higher magnification and boxed area of each channel. (**B** and **D**) SD-ADM images of BafA- or Vac-1–treated osteoblasts. Cells were cultured in osteogenic media containing BafA or Vac-1. (**E**) Alizarin Red S staining performed without fixation. Cells were cultured in osteogenic media containing BafA or Vac-1 and stained with Alizain Red S. Representative confocal images. Scale bars, 50 µm in (A), (C), and (E); 2 µm (B) and (D).

JCRB1119). Primary periodontal ligament cells were isolated and cloned as described previously (*41*). Cells were maintained in α-minimum essential media (Wako Pure Chemical Industries, Japan) containing 10% fetal bovine serum (Thermo Fisher Scientific, MA, USA) and kanamycin (60 µg/ml, Wako Pure Chemical Industries) under normal cell culture conditions (37°C, 5% CO_2). For osteogenic differentiation, the cells were cultured in the same media supplemented with L-ascorbic acid (50 µg/ml) (013-19641, Wako Pure Chemical Industries) and 10 mM β-glycerophosphate (193-02041, Wako Pure Chemical Industries). Calcein [C001, Dojindo, Japan; stock solution (1 mg/ml) was prepared by dilution from stock (50 mg/ml) in 1 M KOH] was incubated at 1 µg/ml for Ca^{2+} imaging during culture with normal or osteogenic media. For mineral staining, cells were fixed with cold 100% ethanol for 5 min and stained with 1.0% Alizarin Red S solution (pH adjusted to 6.4; Wako Pure Chemical Industries, Japan).
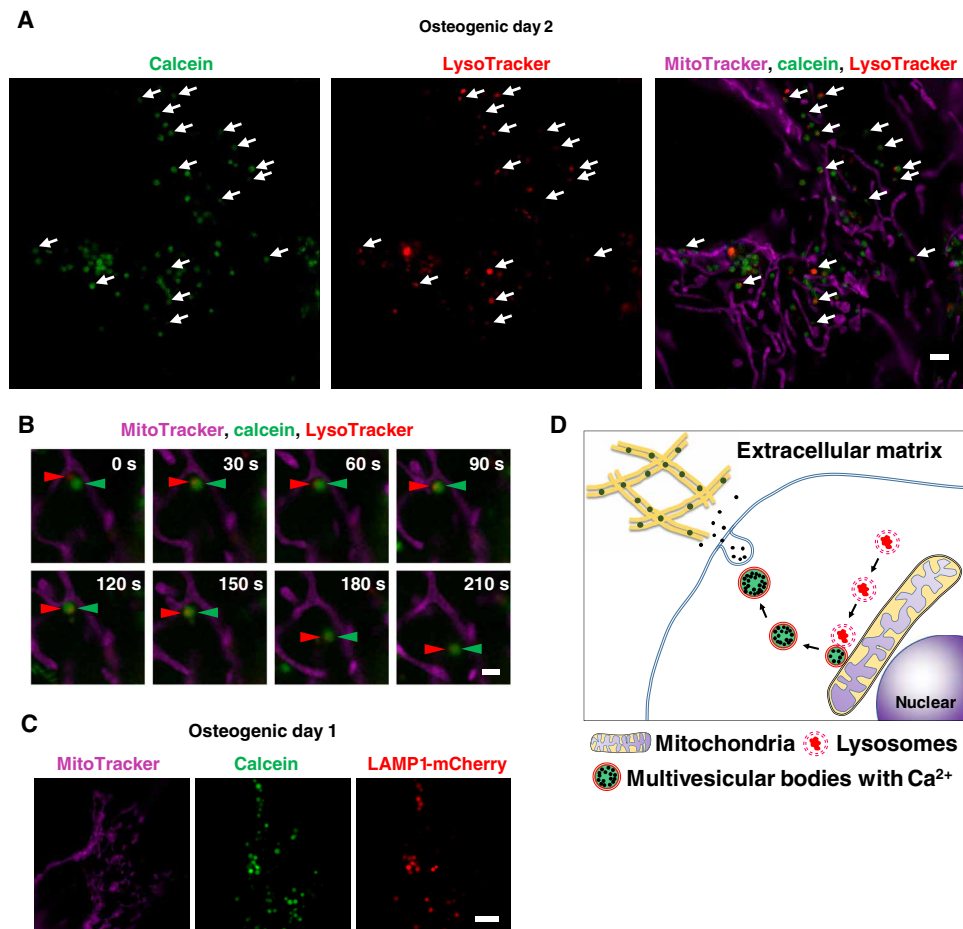
Fig. 4. Super-resolution live imaging of calcium containing vesicle transports via lysosomes. (**A**) Snapshot of time-lapse SRM images of calcein-labeled osteoblasts. Cells were cultured with calcein and stained with Lysotracker and MitoTracker. White arrows indicate colocalization of lysosomes and calcein-positive vesicles. (**B**) Close-up of time-lapse SRM images of calcein-labeled osteoblasts. Red arrowheads indicate lysosome, and green arrowheads indicate calcein. Once lysosomes fused to calcein-positive vesicles adjacent to mitochondria, they started to move toward extracellular space. (**C**) Representative SRM image of LAMP1-mCherry–expressing cells. Cells were transfected with LAMP1-mCherry plasmid, cultured with calcein, and stained with MitoTracker. Calcein-positive vesicles matched to LAMP1-mCherry–positive lysosomes. (D) Schematic view of lysosomal involvement in transportation of calcium in mineralizing osteoblasts. Scale bars, 2 μm in (A), 1 μm in (B), and 10 μm in (C).

Live-cell imaging

pLAMP1-mCherry (*42*) was a gift from A. Palmer (Addgene plasmid no. 45147; http://n2t.net/addgene:45147; RRID: Addgene_45147). The plasmid was transfected with the Neon electroporation system (Thermo Fisher Scientific, MA, USA) using 10-μl tips. The next day, the media was replaced with osteogenic media. The cells, either in osteogenic or normal media, were washed once with phosphate-buffered saline (PBS) and stained with LysoTracker Red DND-99, MitoTracker Deep Red FM, or Hoechst 33342 (Thermo Fisher Scientific) at 1:10,000 for 15 min at 37°C. Subsequently, cells were washed three times with PBS and Live Cell Imaging Solution (Thermo Fisher Scientific) in the presence of ProLong Live Antifade Reagent (Thermo Fisher Scientific). For mineral staining of live cells, a protocol modified from (*43*) was used. In short, live cells were incubated with 0.01% Alizarin Red S solution (Wako Pure Chemical Industries) in culture media for 15 min. Live-cell imaging was performed with the Leica TCS Sp8 confocal microscope (Leica Microsystems, Germany), the N-SIM super-resolution microscope (Nikon Instruments, Japan), or the SpinSR10 spinning disk confocal super-resolution microscope (Olympus Corporation, Japan), according to the manufacturer's instruction.

Western blot analysis

Cells were lysed with radioimmunoprecipitation assay buffer and proteinase inhibitors, and amount of total protein were measured with Bio-Rad protein assay (Bio-Rad, CA, USA) according to the manufacturer's protocol. The samples were prepared with 4× Laemmli sample buffer and 2-mercaptoethanol (Bid-Rad), and SDS–polyacrylamide gel electrophoresis was performed with TGX precast gels (Bio-Rad) and the Mini-PROTEAN electrophoresis system (Bio-Rad). The gel was then transferred to a mini polyvinylidene difluoride membrane with the Trans-Blot Turbo transfer system (Bio-Rad). The membrane was blocked with 5% skim milk in 1× Tris buffered saline with Tween 20 (TBS-T) buffer, and primary and horseradish peroxidase (HRP)–conjugated secondary antibodies were diluted in CanGetSignal solution (TOYOBO, Japan). Following incubation with SuperSignal West Dura Extended Duration Substrate (Thermo Fisher Scientific), chemiluminescence signals were detected with LAS4000 imager (GE Healthcare). Antibodies were obtained as follows: Runx2 (8486S, 1:1000, Cell Signaling Technology Inc., MA, USA), Sp7 (ab22552, 1:1000, Abcam), and HRP-conjugated anti-rabbit immunoglobulin G (IgG) (NA934, 1:10,000; GE Healthcare, IL, USA).

High-resolution SE-ADM

The field-emission SEM (JSM-7000F; JEOL, Tokyo, Japan)–based high-resolution SE-ADM system with the culture dish holder was enabled to observe intact living mammalian cells in media, which was shown in the previous report (15). The liquid-sample holder containing osteoblasts was mounted onto the SEM stage, and the detector terminal was connected to a preamplifier under the holder (44). The electrical signal from the preamplifier was fed into the analog-digital (AD) converter after low-pass filtering, as previously described (45). The Al holder was added to a voltage bias of −8 V. SEM images (1280 × 1020 pixels) were captured at ×3000 to ×50,000 magnification with a scanning time of 80 s with a working distance of 7 mm, an electron beam (EB) acceleration voltage of 4 to 10 kV, and a current of 10 pA.

SE-ADM culture dish holder

A handmade Al holder with a Si frame was attached under a 35-mm culture dish square hole in the center by double-sided tape, as previously described (44). The SE-ADM culture dish holder was subsequently ultraviolet-sterilized for 17 to 18 hours, and osteoblasts were cultured in the dish holder. Next, the Al holder containing cells was separated from the plastic culture dish, attached upside down to another SiN film on an acrylic plate, and sealed (15).

Image processing

SE-ADM signal data from the AD converter were transferred to a personal computer (Intel Core i7, 2.8 GHz, Windows 7), and high-resolution SE-ADM images were processed from the dielectric signal and the scanning signal using the image-processing toolbox of MATLAB R2016b (MathWorks Inc., MA, USA). Original SE-ADM images were filtered using a two-dimensional Gaussian filter (GF) with a kernel size of 7 × 7 pixels and a radius of 1.2σ. Background subtraction was achieved by subtracting SE-ADM images from the filtered images using a broad GF (400 × 400 pixels, 200σ).

Calculation of particle diameters

To calculate the particle size histogram of Fig. 1E, we automatically picked up particle images from the whole SE-ADM image area using MATLAB R2016b (MathWorks Inc.) by an original programmed script. To detect the particle image, we applied a cross-correlation matching method to the SE-ADM image (46). The correlation maps were calculated by a cross-correlation function between template particle images and SE-ADM whole images. The particle images were picked up from peak position in the correlation map. The total numbers of pick-up particle images were 1417, 984, and 1014 on 4, 7, and 10 days, respectively, using the cells cultured in osteogenic media. Then, we automatically calculate each particle diameter using its particle image. Each particle image is processed to intensity reversion and rotation average. Each particle diameter was measured by three-fourth score width in a normalized plot from the particle center. A histogram of particle diameter of Fig. 1E was imaged by GraphPad Prism 7 Software (GraphPad Software, CA, USA).

Immunofluorescence staining of the cells and observation by optical microscopy

In immunofluorescence staining, cells seeded in a 35-mm glass-bottom dish (Matsunami Glass Ind., Ltd., Osaka, Japan) were stained with anti-mouse fibronectin antibody (1:50, BD Biosciences US, CA, USA) or anti-mouse collagen antibody (1:50, Novus Biologicals USA, CO, USA) diluted in a 1:1 mixture of PBS and media (200 μl) for 30 min at 4°C, washed twice with the mixture solution and stained with anti-mouse fluorescein isothiocyanate–conjugated IgG (1:100, Jackson ImmunoResearch Laboratory Inc., Pennsylvania, USA) or anti-rabbit rhodamine-conjugated IgG (1:100, Jackson ImmunoResearch Laboratory Inc.), respectively, diluted in a 1:1 mixture of PBS and media (200 μl) for 30 min at 4°C. After washing twice, the holder was observed under a fluorescence optical microscope.

Immunolabeling of osteoblasts using antibody and 60-nm gold colloids

The KUSA-A1 cells seeded in the dish holder on a 50-nm SiN film were stained with anti-mouse collagen antibody (1:50, Novus Biologicals USA, Colorado, USA) diluted in a 1:1 mixture of PBS and media (50 μl) for 30 min at 4°C, washed twice with the mixture solution, and stained with anti-rabbit IgG-conjugated 60-nm gold colloids (1:50, Cyto-diagnostics Inc., Ontario, Canada) diluted in a 1:1 mixture of PBS and media (50 μl) for 30 min at 4°C. After washing twice, the holder was attached to the acrylic sample holder in the 50-nm SiN film and observed using the SE-ADM system.

EDX spectrometric analysis

SEM images of the SiN film with particles from osteoblasts were observed using JSM-5600LV and JED2140 EDX spectrometric systems (JEOL, Japan) by 15 kV and 50 to 100 pA. The EDX spectroscope data and the element map images were detected by 10 kV and 200- to 300-pA current of EB. The observation times of spectrum and map were 100 and 1000 s, respectively.

Raman microscopy

After fixation with 4% paraformaldehyde, the cell was investigated with a confocal Raman microscope (alpha300R, WITec, Ulm, Germany) using a 532-nm Nd:YAG laser. Spectrum was acquired with a peltier-cooled charge-coupled device detector (DV401-BV, Andor, UK) with 300 gratings/mm (UHTS 600, WITec, Germany). WITec suite (version 5.0, WITec, Germany) was used for data acquisition.

Transfection of CRISPR-Cas9 ribonucleoprotein complex

Guide RNA for each target genes was designed with CRISPRdirect (47) (https://crispr.dbcls.jp/). Target specific CRISPR RNA (crRNA), ATTO550-conjugated trans-activating crRNA (tracrRNA), Cas9 protein were purchased from Integrated DNA Technologies Inc. (IL, USA). Target-specific sequence of crRNA for *Alpl* (NM_007431) without proto-spacer adjacent motif sequence is CTTGCTGTCGC-CAGTAACTG (318-340). Ribonucleoprotein (RNP) complex was formed according to the manufacturer's protocol, and RNPs were transfected to 1×10^5 KUSA-A1 cells using the Neon electroporation system (Thermo Fisher Scientific, MA, USA) with 10-μl tips. Nuclear localization of ATTO550 particles were confirmed on the next day of transfection under a fluorescent microscope (Nikon, Japan).

Single-cell sorting

The RNP transfected cells in six-well plates were harvested with trypsin-EDTA and resuspended in 2% fluorescence correlation spectroscopy containing PBS. Singlet populations were then sorted into 96-well plates with an SH800Z cell sorter (Sony Imaging Products & Solutions Inc., Japan) in a single-cell sorting mode. Recovery rates of each single cell were around 80% when a 130-μm disposable chip (Sony Imaging Products & Solutions Inc.) was used. The sorted cells that formed a visible single colony in each well within a week became ready to be passaged 2 to 3 weeks after sorting.

Measurement of supernatant alkaline phosphatase activity

The 80 μl of 2-week-culture supernatants from single cell–sorted 96-well plates were used to measure alkaline phosphatase activity with the Alkaline Phosphatase Assay Kit (ab83369; Colorimetric, Abcam, Cambridge, UK) according to the manufacturer's instruction.

Quantitative reverse transcription polymerase chain reaction

Total RNA from wild-type and *Alpl* knockout clones were extracted with the PureLink RNA Mini Kit (Thermo Fisher Scientific) 1 day after cells were plated, and complementary DNA was synthesized with SuperScript III reverse transcriptase (Thermo Fisher Scientific) from 1 μg of total RNA according to the manufacturer's instructions. Polymerase chain reaction (PCR) was performed with the StepOnePlus Real-Time PCR System (Applied Biosystems, MA, USA) and Fast SYBR Green Master Mix (Applied Biosystems). The expression level of each gene was normalized to both reference gene (*Hprt1*) and wild type. The primer sets for each target genes were as follows: *Alpl*, NM_007431 (forward) 5′-ctccaaaagctcaacaccaatg-3′ and (reverse) 5′-atttgtccatctccagccg-3′; *Runx2*, NM_009820 (forward) 5′-tggcttg-ggtttcaggttag-3′ and (reverse) 5′-ggtttcttagggtcttggagtg-3′; *Sp7*, NM_130458 (forward) 5′-ggagaccttgctcgtagatttc-3′ and (reverse) 5′-g cagagagacacccacagaac-3′; *Sparc*, NW_009242 (forward) 5′-ggatgggttctgctctcatatt-3′ and (reverse) 5′-cctctgctctggcctta-aatag-3′; *Spp1*, NM_009263 (forward) 5′-ctttcactccaatcgtccctac-3′ and (reverse) 5′-cagaaacctggaaactcctagac-3′; and *Hprt1*, NM_013556 (forward) 5′-ggccagactttgttggatttg-3′ and (reverse) 5′-cgctcatcttag-gctttgtatttg-3′.

Genomic PCR and subcloning for sequencing analysis

Upon passaging the transfected cells, genomic DNA was isolated using the PureLink genomic DNA Mini Kit (Thermo Fisher Scientific). PCR primers for NEBuilder HiFi DNA Assembly (New England BioLabs, MA, USA) were designed with SnapGene 4.1 software (GSL Biotech LLC, IL, USA).

Primers for *Alpl* target region harboring CRISPR-target sites are as follows: (forward) 5′-actaaagggaacaaaagctgcttgggaatggctcctggttt-3′ and (reverse) 5′-actcactataggggcgaattgtgtcctcctgttgcgatgtgtga-3′. Primers for pBluescript KS (+) vector are as follows: (forward) 5′-aaccaggagccattcccaagcagcttttgttcccttagtgaggg-3′ and (reverse) 5′-cacatcgcaacaggaggacacaattcgccctatagtgagtcgt-3′.

PCR-amplified *Alpl* target region, PCR-linearized vector, and NEBuilder HiFi DNA Assembly Master Mix (New England BioLabs) were mixed and incubated at 50°C for 15 min. The mixture was then transformed into NEB5α competent cells (New England BioLabs). The purified DNA from each clone was subject to sequencing analysis.

Inhibitor treatment

BafA (5 mM stock in ethanol; ab120497, Abcam, UK), Vac-1 [40 mM stock in dimethyl sulfoxide (DMSO); 673000-10MG, Merck, Germany], and ES2 (40 mM stock in DMSO; SML1681-5MG, Sigma-Aldrich, MO, USA) were incubated at designated concentrations during culture with normal or osteogenic media.

SUPPLEMENTARY MATERIALS

Supplementary material for this article is available at http://advances.sciencemag.org/cgi/content/full/5/7/eaax0672/DC1

Fig. S1. SE-ADM observation of osteoblasts.
Fig. S2. Extracellular matrix analysis and SE-ADM observation of osteoblasts.
Fig. S3. Generation and characterization of *Alpl* knockout osteoblasts.
Fig. S4. Lysosomal exocytosis inhibitor blocked secretion of calcein-positive vesicles.
Movie S1. Time-lapse SRM movie of calcein labeled osteoblasts.

REFERENCES AND NOTES

1. S. Weiner, L. Addadi, Crystallization pathways in biomineralization. *Annu. Rev. Mat. Res.* **41**, 21–40 (2011).
2. N. Reznikov, J. A. M. Steele, P. Fratzl, M. M. Stevens, A materials science vision of extracellular matrix mineralization. *Nat. Rev. Mater.* **1**, 16041 (2016).
3. H. C. Anderson, Electron microscopic studies of induced cartilage development and calcification. *J. Cell Biol.* **35**, 81–101 (1967).
4. E. Bonucci, Fine structure of early cartilage calcification. *J. Ultrastruct. Res.* **20**, 33–50 (1967).
5. S. Omelon, M. Ariganello, E. Bonucci, M. Grynpas, A. Nanci, A review of phosphate mineral nucleation in biology and geobiology. *Calcif. Tissue Int.* **93**, 382–396 (2013).
6. M. Bottini, S. Mebarek, K. L. Anderson, A. Strzelecka-Kiliszek, L. Bozycki, A. M. S. Simão, M. Bolean, P. Ciancaglini, J. B. Pikula, S. Pikula, D. Magne, N. Volkmann, D. Hanein, J. L. Millán, R. Buchet, Matrix vesicles from chondrocytes and osteoblasts: Their biogenesis, properties, functions and biomimetic models. *Biochim. Biophys. Acta* **1862**, 532–546 (2018).
7. L. Cui, D. A. Houston, C. Farquharson, V. E. MacRae, Characterisation of matrix vesicles in skeletal and soft tissue mineralisation. *Bone* **87**, 147–158 (2016).
8. I. M. Shapiro, W. J. Landis, M. V. Risbud, Matrix vesicles: Are they anchored exosomes? *Bone* **79**, 29–36 (2015).
9. S. Boonrungsiman, E. Gentleman, R. Carzaniga, N. D. Evans, D. W. McComb, A. E. Porter, M. M. Stevens, The role of intracellular calcium phosphate in osteoblast-mediated bone apatite formation. *Proc. Natl. Acad. Sci. U.S.A.* **109**, 14170–14175 (2012).
10. E. Bonucci, Crystal ghosts and biological mineralization: Fancy spectres in an old castle, or neglected structures worthy of belief? *J. Bone Miner. Metab.* **20**, 249–265 (2002).
11. N. Reznikov, M. Bilton, L. Lari, M. M. Stevens, R. Kröger, Fractal-like hierarchical organization of bone begins at the nanoscale. *Science* **360**, eaao2189 (2018).
12. W. J. Landis, M. J. Song, A. Leith, L. McEwen, B. F. McEwen, Mineral and organic matrix interaction in normally calcifying tendon visualized in three dimensions by high-voltage electron microscopic tomography and graphic image reconstruction. *J. Struct. Biol.* **110**, 39–54 (1993).
13. F. Nudelman, K. Pieterse, A. George, P. H. H. Bomans, H. Friedrich, L. J. Brylka, P. A. J. Hilbers, G. de With, N. A. J. M. Sommerdijk, The role of collagen in bone apatite formation in the presence of hydroxyapatite nucleation inhibitors. *Nat. Mater.* **9**, 1004–1009 (2010).
14. J. Mahamid, A. Sharir, D. Gur, E. Zelzer, L. Addadi, S. Weiner, Bone mineralization proceeds through intracellular calcium phosphate loaded vesicles: A cryo-electron microscopy study. *J. Struct. Biol.* **174**, 527–535 (2011).
15. T. Okada, T. Ogura, Nanoscale imaging of untreated mammalian cells in a medium with low radiation damage using scanning electron-assisted dielectric microscopy. *Sci. Rep.* **6**, 29169 (2016).
16. T. Okada, T. Ogura, High-resolution imaging of living mammalian cells bound by nanobeads-connected antibodies in a medium using scanning electron-assisted dielectric microscopy. *Sci. Rep.* **7**, 43025 (2017).
17. S. Matsumoto, I. Shibuya, S. Kusakari, K. Segawa, T. Uyama, A. Shimada, A. Umezawa, Membranous osteogenesis system modeled with KUSA-A1 mature osteoblasts. *Biochim. Biophys. Acta* **1725**, 57–63 (2005).
18. H. C. Anderson, J. B. Sipe, L. Hessle, R. Dhanyamraju, E. Atti, N. P. Camacho, J. L. Millán, R. Dhamyamraju, Impaired calcification around matrix vesicles of growth plate and bone in alkaline phosphatase-deficient mice. *Am. J. Pathol.* **164**, 841–847 (2004).
19. G. Raposo, W. Stoorvogel, Extracellular vesicles: Exosomes, microvesicles, and friends. *J. Cell Biol.* **200**, 373–383 (2013).
20. J. E. Hale, R. E. Wuthier, The mechanism of matrix vesicle formation. Studies on the composition of chondrocyte microvilli and on the effects of microfilament-perturbing agents on cellular vesiculation. *J. Biol. Chem.* **262**, 1916–1925 (1987).
21. M. Rohde, H. Mayer, Exocytotic process as a novel model for mineralization by osteoblasts in vitro and in vivo determined by electron microscopic analysis. *Calcif. Tissue Int.* **80**, 323–336 (2007).
22. J. Mahamid, A. Sharir, L. Addadi, S. Weiner, Amorphous calcium phosphate is a major component of the forming fin bones of zebrafish: Indications for an amorphous precursor phase. *Proc. Natl. Acad. Sci. U.S.A.* **105**, 12748–12753 (2008).
23. J. Mahamid, B. Aichmayer, E. Shimoni, R. Ziblat, C. Li, S. Siegel, O. Paris, P. Fratzl, S. Weiner, L. Addadi, Mapping amorphous calcium phosphate transformation into crystalline mineral from the cell to the bone in zebrafish fin rays. *Proc. Natl. Acad. Sci. U.S.A.* **107**, 6316–6321 (2010).
24. A. L. Boskey, A. S. Posner, Conversion of amorphous calcium phosphate to microcrystalline hydroxyapatite. A pH-dependent, solution-mediated, solid-solid conversion. *J. Phys. Chem.* **77**, 2313–2317 (1973).
25. H. Xu, D. Ren, Lysosomal physiology. *Annu. Rev. Physiol.* **77**, 57–80 (2015).

26. J. Yang, Z. Zhao, M. Gu, X. Feng, H. Xu, Release and uptake mechanisms of vesicular Ca²⁺ stores. *Protein Cell* **10**, 8–19 (2019).

27. T. Hasegawa, Ultrastructure and biological function of matrix vesicles in bone mineralization. *Histochem. Cell Biol.* **149**, 289–304 (2018).

28. M. Kazanci, P. Fratzl, K. Klaushofer, E. P. Paschalis, Complementary information on in vitro conversion of amorphous (precursor) calcium phosphate to hydroxyapatite from Raman microspectroscopy and wide-angle X-ray scattering. *Calcif. Tissue Int.* **79**, 354–359 (2006).

29. J. L. Millán, M. P. Whyte, Alkaline phosphatase and hypophosphatasia. *Calcif. Tissue Int.* **98**, 398–416 (2016).

30. C. Wennberg, L. Hessle, P. Lundberg, S. Mauro, S. Narisawa, U. H. Lerner, J. L. Millán, Functional characterization of osteoblasts and osteoclasts from alkaline phosphatase knockout mice. *J. Bone Miner. Res.* **15**, 1879–1888 (2000).

31. Y. Katsube, N. Kotobuki, M. Tadokoro, R. Kanai, T. Taketani, S. Yamaguchi, H. Ohgushi, Restoration of cellular function of mesenchymal stem cells from a hypophosphatasia patient. *Gene Ther.* **17**, 494–502 (2010).

32. A. L. Boskey, R. Roy, Cell culture systems for studies of bone and tooth mineralization. *Chem. Rev.* **108**, 4716–4733 (2008).

33. S. M. van Gaalen, M. C. Kruyt, R. E. Geuze, J. D. de Bruijn, J. Alblas, W. J. A. Dhert, Use of fluorochrome labels in in vivo bone tissue engineering research. *Tissue Eng. Part B Rev.* **16**, 209–217 (2010).

34. T. Yoshimori, A. Yamamoto, Y. Moriyama, Y. Futai, Y. Tashiro, Bafilomycin A₁, a specific inhibitor of vacuolar-type H⁺ATPase, inhibits acidification and protein degradation in lysosomes of cultured cells. *J. Biol. Chem.* **266**, 17707–17712 (1991).

35. Y. Lu, S. Dong, B. Hao, C. Li, K. Zhu, W. Guo, Q. Wang, K.-H. Cheung, C. W. M. Wong, W.-T. Wu, H. Markus, J. Yue, Vacuolin-1 potently and reversibly inhibits autophagosome-lysosome fusion by activating RAB5A. *Autophagy* **10**, 1895–1905 (2014).

36. C. Zhang, M. Q. Brown, W. van de Ven, Z.-M. Zhang, B. Wu, M. C. Young, L. Synek, D. Borchardt, R. Harrison, S. Pan, N. Luo, Y.-m. M. Huang, Y.-J. Ghang, N. Ung, R. Li, J. Isley, D. Morikis, J. Song, W. Guo, R. J. Hooley, C.-e. A. Chang, Z. Yang, V. Zarsky, G. K. Muday, G. R. Hicks, N. V. Raikhel, Endosidin2 targets conserved exocyst complex subunit EXO70 to inhibit exocytosis. *Proc. Natl. Acad. Sci. U.S.A.* **113**, E41–E50 (2016).

37. L. V. Sutfin, M. E. Holtrop, R. E. Ogilvie, Microanalysis of individual mitochondrial granules with diameters less than 1000 angstroms. *Science* **174**, 947–949 (1971).

38. S. G. Wolf, Y. Mutsafi, T. Dadosh, T. Ilani, Z. Lansky, B. Horowitz, S. Rubin, M. Elbaum, D. Fass, 3D visualization of mitochondrial solid-phase calcium stores in whole cells. *eLife* **6**, e29929 (2017).

39. M. Kerschnitzki, A. Akiva, A. Ben Shoham, Y. Asscher, W. Wagermaier, P. Fratzl, L. Addadi, S. Weiner, Bone mineralization pathways during the rapid growth of embryonic chicken long bones. *J. Struct. Biol.* **195**, 82–92 (2016).

40. Y. C. Wong, D. Ysselstein, D. Krainc, Mitochondria-lysosome contacts regulate mitochondrial fission via RAB7 GTP hydrolysis. *Nature* **554**, 382–386 (2018).

41. Y. Shimabukuro, H. Terashima, M. Takedachi, K. Maeda, T. Nakamura, K. Sawada, M. Kobashi, T. Awata, H. Oohara, T. Kawahara, T. Iwayama, T. Hashikawa, M. Yanagita, S. Yamada, S. Murakami, Fibroblast growth factor-2 stimulates directed migration of periodontal ligament cells via PI3K/AKT signaling and CD44/hyaluronan interaction. *J. Cell Physiol.* **226**, 809–821 (2011).

42. S. B. van Engelenburg, A. E. Palmer, Imaging type-III secretion reveals dynamics and spatial segregation of *Salmonella* effectors. *Nat. Methods* **7**, 325–330 (2010).

43. A. Bensimon-Brito, J. Cardeira, G. Dionísio, A. Huysseune, M. L. Cancela, P. E. Witten, Revisiting in vivo staining with alizarin red S-a valuable approach to analyse zebrafish skeletal mineralization during development and regeneration. *BMC Dev. Biol.* **16**, 2 (2016).

44. T. Ogura, Nanoscale analysis of unstained biological specimens in water without radiation damage using high-resolution frequency transmission electric-field system based on FE-SEM. *Biochem. Biophys. Res. Commun.* **459**, 521–528 (2015).

45. T. Ogura, Direct observation of unstained biological specimens in water by the frequency transmission electric-field method using SEM. *PLOS ONE* **9**, e92780 (2014).

46. T. Ogura, C. Sato, An automatic particle pickup method using a neural network applicable to low-contrast electron micrographs. *J. Struct. Biol.* **136**, 227–238 (2001).

47. Y. Naito, K. Hino, H. Bono, K. Ui-Tei, CRISPRdirect: Software for designing CRISPR/Cas guide RNA with reduced off-target sites. *Bioinformatics* **31**, 1120–1123 (2015).